other morphological changes that reflect an earlier automatic response on the part of the plants to the selective pressures of seedbed and harvesting (the adaptive syndrome of domestication) (*1, 2, 17*). The intact *Cucurbita* seeds from the Archaic period occupations of the cave provide evidence, in terms of size increase, that such an adaptive response to seedbed selective pressures had occurred by ca. 9000 ^{14}C years B.P. (ca. 10,000 calendar years B.P.) In the initial analysis of the *Cucurbita* assemblage from the cave (*9*), no clear morphological criteria were stated for assigning domesticated status to the Guilá Naquitz *Cucurbita* seeds, including the single seed recovered from zone D that was identified as domesticated. An increase in size above that documented for wild seeds has been the standard criterion for identifying the seeds of domesticated *C. pepo* (*11–13, 17*). The 35 late Pleistocene (ca. 12,500 ^{14}C years B.P.) seeds of a wild *Cucurbita* gourd recently recovered from American mastodon (*Mammut americanum*) dung deposits at the Page-Ladson site in Florida (*12*) provide a good wild baseline of comparison. The single seed from zone D of Guilá Naquitz has length and width dimensions (10 by 7 mm) that fall close to the average values (9.87 by 6.62 mm) of the Page-Ladson wild seed assemblage (range 8.73 to 11.15 mm and 5.07 to 7.60 mm), and thus it cannot be considered as evidence for the presence of domesticated *C. pepo*. Of the five measured seeds from zone C of Guilá Naquitz, four fall within or close to the upper end of the Page-Ladson size range in terms of length, although one has a length of 13.8 mm (Table 1 and Figs. 1 and 2C). The AMS ^{14}C date on this largest of the zone C seeds is 8910 ^{14}C years B.P. (ca. 9900 calendar years B.P.) (Table 1 and Fig. 1). Seven of the eight zone B seeds also exceed the size range of the wild comparative baseline population (range 11.4 to 17.0 mm) (Fig. 1). Samples from five of these seven large zone B seeds have AMS ^{14}C ages of 7610 to 8990 ^{14}C years B.P. (ca. 8400 to 10,000 calendar years B.P.) (Table 1 and Fig. 1). The largest and oldest of these dated zone B seeds was comparable in both size and age to the AMS-dated zone C seed. Taken together, these two seeds, both of which exhibit marginal ridge and hair characteristics diagnostic for *C. pepo* (*3*) (Fig. 2C) and are 18 to 24% larger than the largest of the wild baseline Page-Ladson seeds, imply the presence of domesticated *C. pepo* ssp. *pepo* in Guilá Naquitz cave by ca. 9000 ^{14}C years B.P. (ca. 10,000 calendar years B.P.).

The temporal and developmental pattern of automatic adaptive response (increase in seed size) preceding deliberate human selection (change in fruit shape and color) in the Guilá Naquitz squash closely parallels the developmental sequence documented for the domestication of the other major lineage of *C. pepo* squash (*C. pepo* ssp. *ovifera*) in eastern North America, in which an increase in seed size preceded any changes in fruit morphology (*11, 16*). The domesticated *C. pepo* from Guilá Naquitz opens up considerable room for debate regarding the timing, context, and causes of agricultural origins in Mesoamerica, while also underscoring the need for further excavation of early agricultural cave and river valley settlements of the Archaic period in different regions of Mexico.

REFERENCES AND NOTES

1. B. D. Smith, *The Emergence of Agriculture* (Scientific American Library, New York, 1995).
2. P. K. Bretting, Ed., *Econ. Bot.* **44** (suppl.) (1990).
3. B. D. Smith, *Latin Am. Antiq.*, in press.
4. D. S. Byers, Ed., *The Prehistory of the Tehuacán Valley* (Univ. of Texas Press, Austin, TX, 1967), vol. 1.
5. K. V. Flannery, Ed., *Guilá Naquitz* (Academic Press, Orlando, FL, 1986).
6. L. Kaplan, "Accelerator dates and the antiquity of *Phaseolus*," paper presented at the annual meeting of the Society for Economic Botany, Miami, FL, 23 to 27 June 1993; "*Phaseolus* beans, accelerator dates in the Americas," paper presented at the annual meeting of the Society for American Archaeology, Minneapolis, MN, 3 to 7 May 1995.
7. A. Long, B. Benz, D. Donahue, A. Jull, L. Toolin, *Radiocarbon* **3**, 1035 (1989).
8. G. A. Fritz, *Curr. Anthropol.* **35**, 305 (1994); B. D. Smith, *Evol. Anthropol.* **3**, 174 (1995).
9. T. Whitaker and H. Cutler, in (*5*), pp. 275–279.
10. The Guilá Naquitz cucurbit assemblage is now curated at the Laboratorio de Paleobotánica, Instituto Nacional de Antropología e Historia (INAH), Mexico, Distrito Federal. The rind, seed, and peduncle specimens illustrated in the original analysis (*9*) are not present in the INAH collections. As a result, the rind and peduncle specimens illustrated in (*9*) are not included in this analysis. Seed measurements provided in (*9*), however, are included in Fig. 1.
11. C. W. Cowan and B. D. Smith, *J. Ethnobiol.* **13**, 17 (1993).
12. L. A. Newsom, S. D. Webb, J. S. Dunbar, *ibid.*, p. 75.
13. F. King, *Anthropol. Pap. Mus. Anthropol. Univ. Mich.* **75**, 73 (1985).
14. L. C. Merrick and D. M. Bates, *Baileya* **23**, 94 (1989).
15. The as yet undated large peduncle from zone C (Fig. 1) may indicate an even earlier increase in fruit size, given that it is from the same provenience (E9) as the domesticated *C. pepo* seed that yielded an AMS radiocarbon date of 8910 ^{14}C years B.P. (Table 1 and Figs. 1 and 2C).
16. D. Decker, *Econ. Bot.* **42**, 4 (1988); D. Decker-Walters, T. W. Walters, C. W. Cowan, B. D. Smith, *J. Ethnobiol.* **13**, 55 (1993).
17. J. R. Harlan, J. M. J. deWet, E. G. Price, *Evolution* **27**, 311 (1973).

18. Figure 1 is by M. Bakry and Fig. 2 photographs are by C. Hansen. I thank INAH for permission to sample Guilá Naquitz specimens for AMS ^{14}C dates; F. Sànchez, director of the Laboratorio de Paleobotánica, INAH, and J. L. Alvarado for their kind hospitality and their consultation on the analysis; J. L. Alvarado, D. Decker-Walters, K. Flannery, G. Fritz, L. Kaplan, L. Newsom, F. Sanchez, P. J. Watson, and M. Zeder for comments on the manuscript; and Y. Sugiura and C. Castillo, without whose assistance this research would not have been possible.

28 January 1997; accepted 4 March 1997

North and Northeast Greenland Ice Discharge from Satellite Radar Interferometry

E. J. Rignot,* S. P. Gogineni, W. B. Krabill, S. Ekholm

Ice discharge from north and northeast Greenland calculated from satellite radar interferometry data of 14 outlet glaciers is 3.5 times that estimated from iceberg production. The satellite estimates, obtained at the grounding line of the outlet glaciers, differ from those obtained at the glacier front, because basal melting is extensive at the underside of the floating glacier sections. The results suggest that the north and northeast parts of the Greenland ice sheet may be thinning and contributing positively to sea-level rise.

The traditional view on the mass balance of the Greenland ice sheet is that accumulation of mass (mostly snow) in the interior regions is released to the ocean through surface ablation (or melting) and calving of icebergs (*1*). Of all three components of the mass balance, snow accumulation is the best known from measurements of snow pits and ice cores across the ice sheet (*2*). Observations of surface melt rates are comparatively limited and restricted to the western marginal zone (*3*). Iceberg calving is the least known of the components (*4*). Iceberg production has been estimated in the west (*5*), north, and northeast (*6*) of Greenland by means of repeated aerial photography. The velocity of the calving front is measured by tracking distinctive patterns of crevasses over time. Ice thickness is deduced from the height of the calving front. Immediately inland of the calving front, ice thickness is not well known (*7*), surface features are more subdued, and locating the grounding line, which is where a glacier detaches

E. J. Rignot, Jet Propulsion Laboratory, California Institute of Technology, 4800 Oak Grove Drive, Pasadena, CA 91109–8099, USA.
S. P. Gogineni, Radar Systems and Remote Sensing Laboratory, The University of Kansas, 2291 Irving Hill Road, Lawrence, KS 66045–2969, USA.
W. B. Krabill, NASA Goddard Space Flight Center, Wallops Flight Facility, Laboratory for Hydrospheric Processes, Wallops Island, VA 23337, USA.
S. Ekholm, Kort and Matrikelstyrelsen, Geodetic Division, Rentemestervej 8, DK-2400 Copenhagen NV, Denmark

*To whom correspondence should be addressed. E-mail: eric@adelie.jpl.nasa.gov

from its bed to become afloat in the ocean, is difficult (*8*).

Satellite radar interferometry permits a systematic, detailed, and precise mapping of the grounding line of outlet glaciers (*9*, *10*). The grounding line is a natural boundary for calculating ice discharge because the entire ice volume that crosses it eventually melts into the ocean. We mapped the grounding line of north and northeast Greenland glaciers (Figs. 1 and 2) (*11*), using radar data from the Earth Remote Sensing satellites (ERS-1 and ERS-2), and estimated their ice discharge at the grounding line. This part of Greenland includes large sections of floating glacier ice, which are preserved because of the low glacier slopes combined with the constraining effect of permanent sea ice in the fjords (*12*).

We used a high-quality digital elevation model (DEM) of north Greenland (*13*) to estimate the thickness of the floating glacier sections in this region, assuming that the glacier ice is in hydrostatic equilibrium (*14*). To assess the accuracy of the method, we compared the elevation data to ice thickness data obtained by an ice sounding radar (ISR) (*15*) and to laser altimetry data (AOL) (*16*) collected along single longitudinal profiles crossing the grounding line of the three largest glaciers (Figs. 2 and 3). The comparison shows that hydrostatic equilibrium is first reached about 1 to 2 km downstream from the interferometrically derived grounding line or hinge line (*11*). Near that location, the DEM-derived thickness is within 10% of the AOL-derived thickness and the ISR data.

Ice discharge was calculated along profiles located 1 km downstream from the hinge line and parallel to it, as the integral of the product of the DEM-derived ice thickness with the velocity component perpendicular to the grounding line. Over the floating section of a glacier, the vertical gradient in velocity is negligible (*17*), so the ERS-derived velocities represent vertically integrated velocities. The actual ice velocity vectors were obtained by combining the line-of-sight component of the velocity procured by radar interferometry with flow direction information provided by the prominent glacier flow lines in the radar amplitude images (Fig. 2). The precision of the measured perpendicular component of the ice velocity is 4% (*18*).

Combined together, the analysis implies

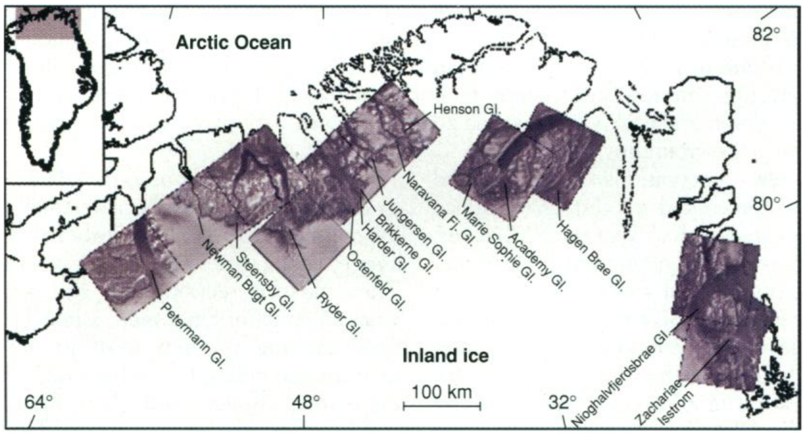

Fig. 1. Location of the 14 outlet glaciers of north and northeast Greenland and the ERS frames used in this study. Each ERS scene is 100 km². Gl., Gletscher; Fj., fjord.

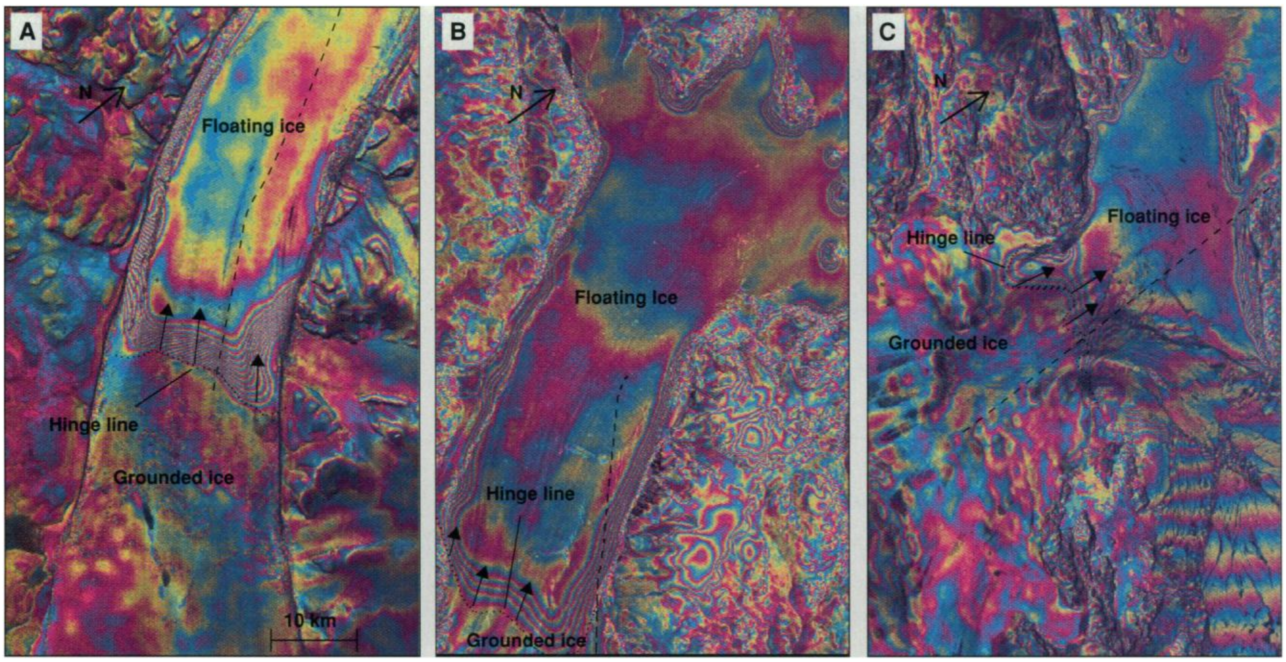

Fig. 2. Tidal displacements of the floating section of (**A**) Petermann Gletscher, (**B**) Nioghalvfjerdsbræ Gletscher, and (**C**) Zachariae Isstrøm obtained from quadruple-difference ERS radar interferometry. Each fringe, or 360° variation in phase, represents a 28-mm displacement of the glacier tongue toward the radar line of sight (23° away from vertical) due to forcing by the ocean tide. The phase image is modulated by the radar brightness of the scene. The hinge line, or limit of tidal flexing, is shown as a dotted line. The amplitude of the tidal displacements raises quickly from the hinge line (high fringe rate)and subsequently decreases slowly toward the glacier front. This deformation pattern agrees with model predictions from an elastic beam clamped at one end on bedrock (hinge line) and freely floating on the ocean (*24*). The location of the ISR and AOL profiles for each glacier is shown in dashes. North (N) is indicated by an arrow. Solid arrows indicate flow direction parallel to flow lines conspicuous in the radar amplitude images. Residual fringes on rock are caused by imperfections in the DEM in areas of high topographic relief.

that the 14 glaciers discharge 49.2 km^3/year of ice into the ocean (10% uncertainty) (Table 1). This ice volume is 3.5 times that discharged at the glacier front (6). The largest difference is recorded on Petermann Gletscher, where the grounding line flux is 22 times the glacier-front flux.

If the floating glacier sections are in steady-state conditions, the ice flux decrease implies that they are melting (19). If they are not in steady state, they should be thickening instead, because not enough ice passing the grounding line reaches the glacier front. AOL data collected in 1995 and 1996 on Petermann Gletscher, however, indicate that the glacier tongue did not thicken at detectable levels (>1 m) over 1 year. Therefore, we assume that the ice tongue is in steady state and the ice flux decrease is due to melting. On Petermann Gletscher, the inferred steady-state melt rate is 12 m/year, and peak values exceed 20 m/year near the grounding line (10).

The few observations in north and northeast Greenland suggest that surface melt rates are less than 3 m/year (20). Thus, the only possible explanation for the ice-flux decrease is that the ice tongues lose mass through extensive melting at the base of the glaciers. If we assume a surface melt rate of 2 m/year for the floating tongues (6), basal melting must average 10 m/year on Petermann Gletscher, 8 m/year on Nioghalvfjerdsbræ Gletscher, and 6 m/year on Zachariae Isstrøm to explain the results in Table 1. These values are high compared with the 1 to 2 m/year average basal melt rate of Antarctic ice shelves (21), but are comparable to the localized high basal melt rates (7 to 10 m/year) measured on several Antarctic tidal outlet glaciers (22).

The outlet glaciers of north and northeast Greenland will maintain a state of balance if the mass discharged at the grounding line is compensated by an equal amount of mass accumulating in the interior regions, which nourishes them with glacier ice. Over our study area, the predicted balance grounding line discharge for an ice sheet in balance is 41 km^3/year (23), which is less than the discharge of 49 km^3/year measured with the ERS data. If these estimates are correct, this means that north and northeast Greenland glaciers discharge an excess 8 km^3/year of glacier ice into the ocean, which is equivalent to a 7-Gt/year mass loss (with an ice density of 0.917), a 0.02-mm sea-level rise, or a decrease of 2.5 cm/year in surface elevation averaged over the total area above the grounding line (332,100 km^2). The northern sector of the Greenland Ice Sheet is therefore thinning and gives a positive contribution to sea-level rise.

Our results cannot be extrapolated easily to the entire ice sheet because small floating glacier sections exist elsewhere—for example, along the western coast (5, 12). These floating sections may still generate large amounts of basal melt water, because basal melting is often most pronounced near the grounding line, where tidal pumping is most efficient and where the glacier draft reaches the deepest waters (21, 22).

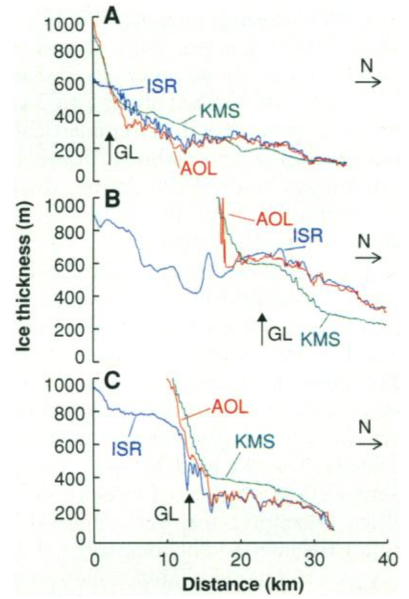

Fig. 3. Ice thickness derived from AOL, ISR, and surface elevation (KMS) near the grounding line (GL, indicated by an arrow) of (**A**) Petermann Gletscher, (**B**) Nioghalvfjerdsbræ Gletscher, and (**C**) Zachariae Isstrøm, as a function of the distance along the profile. North (N) is indicated by an arrow. The precision of the KMS elevation, AOL elevation, and ISR thickness is, respectively, 10 to 20 m (13), 10 cm (16), and 10 m (15). Georeferencing of the ERS data is accurate to within 80 m. The AOL/ISR profile for Nioghalvfjerdsbræ Gletscher is not optimal because it is too close to the ice margin and almost parallel to the grounding line (Fig. 2). The AOL- and KMS-derived thicknesses calculated upstream (south) of the grounding line are in error because the glacier ice is not in hydrostatic equilibrium.

Table 1. Glacier width (W), average velocity (V), average thickness (T), grounding line ice flux (GF), and calving flux (CF) from (6) for the outlet glaciers in Fig. 1. W, V, and T for Ostenfeld Gletscher and Brikkerne Gletscher are for the main glacier branch only. The last line indicates total ice discharge. Gl., Gletscher; Fj., fjord.

Glacier	W (km)	V (m/year)	T (m)	GF (km^3/year)	CF (km^3/year)
Petermann Gl.	20.5	1139	614	13.20	0.59
Steensby Gl.	3.4	329	547	0.63	0.32
Ryder Gl.	7.9	506	598	2.55	0.70
Ostenfeld Gl.	7.6	667	544	2.71	0.54
Harder Gl.	4.5	187	340	0.34	0.03
Brikkerne Gl.	3.8	364	160	0.44	0.37
Jungersen Gl.	1.5	395	340*	0.20	0.10
Naravana Fj. Gl.	1.8	59	200*	0.02	0.01
Henson Gl.	2.2	286	123*	0.08	0.04
Marie Sophie Gl.	3.3	40	136	0.02	0.13
Academy Gl.	7.4	290	120	0.26	0.14
Hagen Brae Gl.	7.9	111	731	0.64	0.36
Nioghalvfjerdsbræ Gl.	21.5	1022	771	15.74	2.80†
Zachariae Isstrøm	19.8	855	647	12.40	7.40†
Total				49.2	13.5

*Uncertainties in ice thickness greater than 10%. †Calving flux from (25).

REFERENCES AND NOTES

1. N. Reeh, in *Quaternary Geology of Canada and Greenland*, R. J. Fulton, Ed. (Geological Survey of Canada, Geology of Canada, 1989), chap. 14, pp. 793–822; C. S. Benson, *U.S. Army Cold Reg. Res. Eng. Lab. Rep. 70* (Hanover, NH, 1962); A. Weidick, *Gletscher-Hydrol. Medd.* **85**, (1985); H. Bader, *U.S. Army Cold Reg. Res. Eng. Lab. Rep. I-B2* (Hanover, NH, 1961); F. Loewe, *Beitr. Geophys.* **46**, 317 (1936).
2. A. Ohmura and N. Reeh, *J. Glaciol.* **37**, 140 (1991).
3. R. Braithwaite, *Groenl. Geol. Undersoegelse* **98**, 1 (1980).
4. N. Reeh, *Glaciers, Ice Sheets, and Sea Level: Effects of a CO_2-Induced Climatic Change*, Seattle, WA, 13 to 15 September 1984 (National Academy Press, Washington, DC, 1985), pp. 155–171.
5. M. Carbonnell and A. Bauer, *Medd. Groenl.* **173**, 1 (1968); R. C. Kollmeyer, *Cold Reg. Sci. Technol.* **1**, 175 (1980).
6. A. Higgins, *Groenl. Geol. Undersoegelse* **140**, 1 (1988); *Polarforschung* **60**, 1 (1990).
7. P. Gudmandsen, in *Remote Sensing of the Terrestrial Environment 28*, R. F. Peel, L. F. Curtis, E. C. Barret, Eds. (Colston Papers, Bristol, UK, 1977), pp. 198–211.
8. The grounding line may be located from an examination of small fractures at the surface of a glacier caused by the tidal displacements [S. N. Stephenson, *Ann. Glaciol.* **5**, 165 (1984)], or using a radio echo sounder [R. W. Jacobel, A. E. Robinson, R. A. Bindschadler, *ibid.* **20**, 39 (1994)]. The limit of tidal flexing is precisely found with global positioning system (GPS) surveys and tiltmeters [D. G. Vaughan, *ibid.*, p. 372; A. M. Smith, *J. Glaciol.* **37**, 51 (1991)]. The above techniques, however, are limited in spatial sampling. Visible imagery [C. Swithinbank, K. Brunk, J. Sievers, *Ann. Glaciol.* **11**, 150 (1988)] and radar altimetry [R. H. Thomas, T. V. Martin, H. J. Zwally, *ibid.* **4**, 283 (1983)] provide a large-scale, uniform sampling view of the grounding zone, but their precision is much less than that of GPS techniques.
9. R. M. Goldstein, H. Engelhardt, B. Kamb, R. M.

Frolich, *Science* 262, 1525 (1993).
10. E. Rignot, *J. Glaciol.* 42, 476 (1996).
11. To locate the grounding line with ERS radar interferometry, we used two interferograms formed by combining ERS image data acquired 1 day apart. A DEM was registered to each interferogram from a knowledge of the radar imaging geometry and the satellite precision orbits. The phase variations associated with surface topography and the interferometric baseline were then automatically removed from the interferograms, leaving only phase variations caused by the glacier deformation over 1 day. This deformation is the combination of a long-term motion under the driving stress procured by gravity, and a short-term vertical motion induced by tidal forcing from the ocean. If the glacier velocity (or gravity term) is continuous and steady throughout the period of observation, the differencing of two such interferograms produces a third interferogram which only contains the tidal signal. It is then possible to locate the limit of tidal flexing, or glacier hinge line, within less than 100 m, across the entire glacier width (*10*).
12. L. Koch, *Medd. Groenl.* 65, 181 (1928).
13. S. Ekholm, *J. Geophys. Res.* 101, 21961 (1996).
14. An accurate measurement of the ice thickness from the glacier surface elevation requires a knowledge of the density profile with depth. We assumed that the mean glacier ice density, ρ_i, is 917 kg/m^3 for the relatively warm ice of the coastal regions [P. V. Hobbs, *Ice Physics* (Oxford Univ. Press, London, 1974)], and the sea water density, ρ_w, is 1030 kg/m^3 [A. Foldvik, T. Gammelsrød, T. Tørresen, *Polar Res.* 3, 209 (1985)]. Ice thickness is obtained by multiplying the surface elevation by $\rho_w/(\rho_w-\rho_i)$, or 9.115.
15. T. S. Chuah, S. P. Gogineni, C. Allen, B. Wohletz, *Radar Systems and Remote Sensing Laboratory Technical Report 10470* (University of Kansas, Lawrence, KS, 1996).
16. W. B. Krabill, R. H. Thomas, C. F. Martin, R. N. Swift, E. B. Frederick, *Int. J. Remote Sens.* 16, 1211 (1995).
17. T. J. O. Sanderson and C. S. M. Doake, *J. Glaciol.* 22, 285 (1979).
18. Ice flow direction is known within 5°. The line-of-sight interferometric velocity is known within 2 mm/day or 1 m/year. The ERS data had a line-of-sight vector within 30° of the main flow direction.
19. W. S. B. Paterson, *The Physics of Glaciers* (Elsevier Science, Tarrytown, NY, 1994).
20. C. E. Bøggild, N. Reeh, H. Oerter, *Global Planet. Change* 9, 79 (1994); T. Konzelmann and R. Braithwaite, *J. Glaciol.* 41, 174 (1995); T. Høy, *Medd. Groenl.* 182, 1 (1970).
21. S. S. Jacobs, H. H. Helmer, C. S. M. Doake, A. Jenkins, R. M. Frolich, *J. Glaciol.* 38, 375 (1992); A. Jenkins and C. S. M. Doake, *J. Geophys. Res.* 96, 791 (1991); D. R. McAyeal, *ibid.* 89, 597 (1984).
22. S. S. Jacobs, H. H. Helmer, A. Jenkins, *Geophys. Res. Lett.* 23, 957 (1996); A. M. Smith, *J. Geophys. Res.* 101, 22749 (1996).
23. The total accumulation volume of the 14 glaciers in the region above the grounding line is 57 km^3/year, derived from the DEM in (*13*), the accumulation data in (*2*), and an ice density of 0.917. Surface ablation over the same area amounts to 16 km^3/year, as calculated from the positive degree-day model [N. Reeh, *Polar Forsch.* 59, 113 (1991)] and a degree-day factor of 9.8 mm degree^{-1} day^{-1} [T. Konzelmann and R. J. Braithwaite, *J. Glaciol.* 41, 174 (1995)]. The balance discharge at the grounding line is therefore 41 km^3/year.
24. G. Holdsworth, *J. Glaciol.* 8, 385 (1969); *Ann. Geophys.* 33, 133 (1977).
25. A. Weidick, *U.S. Geol. Surv. Prof. Pap. 1386* (Denver, CO, 1995).
26. We thank G. Duchossois, G. Kohlhammer, and the European Space Agency for providing radar data; R. H. Thomas for useful discussions; and C. Werner for providing a synthetic-aperture radar processor. This work was carried out at the Jet Propulsion Laboratory, California Institute of Technology, under a contract with NASA.

16 January 1997; accepted 5 March 1997

Surface Composition of Kuiper Belt Object 1993SC

Robert H. Brown, Dale P. Cruikshank, Yvonne Pendleton, Glenn J. Veeder

The 1.42- to 2.40-micrometer spectrum of Kuiper belt object 1993SC was measured at the Keck Observatory in October 1996. It shows a strongly red continuum reflectance and several prominent infrared absorption features. The strongest absorptions in 1993SC's spectrum occur near 1.62, 1.79, 1.95, 2.20, and 2.32 micrometers in wavelength. Features near the same wavelengths in the spectra of Pluto and Neptune's satellite Triton are due to CH_4 on their surfaces, suggesting the presence of a simple hydrocarbon ice such as CH_4, C_2H_6, C_2H_4, or C_2H_2 on 1993SC. In addition, the red continuum reflectance of 1993SC suggests the presence of more complex hydrocarbons.

Ever since Kuiper (*1*) postulated a remnant population of solar system objects just beyond the orbit of Pluto, there has been speculation as to the existence and nature of these objects, as well as to whether they are representative of the small bodies from which all the known planets are thought to have arisen. Because the Kuiper belt objects (KBOs) were thought to be mostly beyond the range of planetary perturbations, and because they were thought to be too tightly bound to the sun to be perturbed by passing stars, it was hypothesized that KBOs may be primitive remnants of the early solar system (*1*, *2*). In contrast, the Oort cloud, a halo of objects believed to be the source of long-period comets and assumed to extend out to the limits of the sun's gravitational sphere (*3*), may be populated primarily by objects ejected from the region of the giant planets (*4*). Thus, KBOs may not have been as strongly heated as objects populating the Oort cloud and as a result may have unique surface compositional characteristics. KBOs are important to our understanding of the chemistry of the early solar system, but their distance and small size (less than a few hundred kilometers in diameter) precluded discovery until recently. Within the last 4 years, however, over 40 objects have been discovered (*5*). In fact, the Kuiper belt may have $>10^8$ objects larger than 10 km in diameter (*6*).

Detailed here are near-infrared spectroscopic observations of the Kuiper belt object 1993SC, and the implications that these observations have for its surface composition. The observations were conducted at the W. M. Keck Observatory during the period 2 to 4 October 1996 universal time (UT). The Keck I telescope was used with the near-infrared camera (NIRC) as the focal plane instrument. The observations were conducted with the gr120 grism of the NIRC, which has an effective wavelength range in first order of 1.45 to 2.55 μm and a spectral sampling interval of 0.007 μm. The NIRC has an effective pixel size of 0.15 arc sec, and a slit width of 8 pixels (1.2 arc sec) was used for all the spectral observations.

We located 1993SC using the latest orbital elements (*7*) in the commercially available ephemeris program Ephem (*8*) and identified the object in an image taken through the NIRC's K_s filter (*9*). The telescope was then offset 5 arc sec to the north to obtain an additional image and a measurement of the night sky brightness, while tracking the predicted motion of 1993SC. The resulting series of positive-negative pairs in the differenced images showed different apparent position angles, depending on whether or not an object was moving at the sidereal rate. In addition to the position angle difference, objects moving at sidereal rate were trailed. That 1993SC was moving against the stellar background at the predicted rate was corroborated in a final image acquired some 20 min after the initial image, which allowed a check of the total movement of the object against the stellar background.

Collecting a spectrum involved positioning the object in the center of the slit and obtaining pairs of images of 1800 s total exposure (18 separate exposures of 100 s co-added) with each exposure offset along the grism slit by 5 arc sec, alternately north then south. Differencing corresponding pairs of images allowed an accurate subtraction of the sky background

R. H. Brown, Lunar and Planetary Laboratory and Steward Observatory, University of Arizona, Tucson, AZ 85721, USA.
D. P. Cruikshank and Y. Pendleton, NASA Ames Research Center, Moffett Field, CA 94035, USA.
G. J. Veeder, Jet Propulsion Laboratory, California Institute of Technology, Pasadena, CA 91109, USA.